ATLAS Paper Draft
EXOT-2018-14
Version 2.0
Target journal: Phys. Rev. D

Comments are due by: 28 June 2023

Supporting internal notes

QBH: https://cds.cern.ch/record/2637190

Search for quantum black hole production in lepton+jet final states using proton–proton collisions at $\sqrt{s} = 13$ TeV with the ATLAS detector

A search for quantum black holes in electron+jet and muon+jet invariant mass spectra is performed with 140 fb^{-1} of data collected by the ATLAS detector in proton–proton collisions at $\sqrt{s} = 13$ TeV at the Large Hadron Collider. The observed invariant mass spectrum of lepton+jet pairs is consistent with Standard Model expectations. Upper limits are set at 95% confidence level on the production cross-sections times branching fractions for quantum black holes decaying into a lepton and a quark in a search region with invariant mass above 2.0 TeV. The resulting quantum black hole lower mass threshold limit is 9.2 TeV in the Arkani-Hamed-Dimopoulos-Dvali model, and 6.8 TeV in the Randall-Sundrum model.

Document created on June 21, 2023 using ATLAS LaTeX Version 14.3.0.

Analysis Team

[*email:* atlas-EXOT-2018-14-editors@cern.ch]

D. Gingrich, S. Karpov, Z. Karpova

ATLAS Paper

EXOT-2018-14

June 21, 2023

Journal: Phys. Rev. D

Draft version 2.0

Search for quantum black hole production in lepton+jet final states using proton–proton collisions at $\sqrt{s} = 13$ TeV with the ATLAS detector

The ATLAS Collaboration

A search for quantum black holes in electron+jet and muon+jet invariant mass spectra is performed with 140 fb^{-1} of data collected by the ATLAS detector in proton–proton collisions at $\sqrt{s} = 13$ TeV at the Large Hadron Collider. The observed invariant mass spectrum of lepton+jet pairs is consistent with Standard Model expectations. Upper limits are set at 95% confidence level on the production cross-sections times branching fractions for quantum black holes decaying into a lepton and a quark in a search region with invariant mass above 2.0 TeV. The resulting quantum black hole lower mass threshold limit is 9.2 TeV in the Arkani-Hamed-Dimopoulos-Dvali model, and 6.8 TeV in the Randall-Sundrum model.

1 Introduction

Quantum black holes (QBHs) are predicted in low-scale quantum gravity models [1–3] that offer solutions to the mass hierarchy problem of the Standard Model (SM) by lowering the scale of quantum gravity (M_{D}) from the Planck scale ($\sim 10^{16}$ TeV) to the TeV region (1–10 TeV or more). In this case, gravity becomes strong and quantum effects are relevant. In models with large extra dimensions such as the Arkani-Hamed-Dimopoulos-Dvali (ADD) model [1, 2], the gravitational field is allowed to propagate in n extra dimensions, while all SM fields are localized in the usual four-dimensional space-time. There are also warped scenarios, such as the Randall-Sundrum model (RS1) [3], in which a single warped extra dimension separates two three-dimensional branes by some distance. Gravitons can propagate in this warped dimension, and the effective Planck scale on the three-dimensional brane is determined by the curvature of the extra dimension, also referred to as the warp factor. These models postulate conservation of total angular momentum, color, and electric charge in the production and in the decay of QBHs [4–6]. The behavior of QBHs with masses near M_{D} decaying into two-particle final state is distinct from that of the semi-classical black holes [7] that decay into a multi-particle final state via Hawking radiation [8–11]. Two-particle final state exceeds 50% of all possible QBH decay outcomes including 3, 4, and more particles [6].

The threshold mass, M_{th}, for QBH production, is set equal to M_{D} during the event generation, to ensure that the QBHs are produced in the region in which expected quantum effects are important. A test of QBH models is accessible at the Large Hadron Collider (LHC) up to $M_{\mathrm{th}} \lesssim 13$ TeV. A search for QBHs decaying into a single electron (e) or a single muon (μ), and a quark producing a jet is undertaken in this paper. The QBHs are postulated to be produced near the M_{D} (2–10 TeV). The QBH simulation assumes massless partons and conserves total angular momentum. The initial angular momentum of the QBH is entirely due to the spin states of the incoming partons. The initial orbital angular momentum can be neglected due to a tiny impact parameter in the parton-parton collision. Thus, the QBH in this analysis can only be produced either in the spin-0 or the spin-1 state. The strong-gravity interactions do not necessarily preserve the same symmetries as does the SM. Although one might expect angular momentum, electric charge, and color to be conserved, it is less clear that global symmetries such as baryon or lepton number of the SM need to be conserved in strong-gravity interactions. While in high Planck-scale gravity in four dimensions the baryon number violation is bound to be very small, the baryon number violation in low-scale gravity in higher dimensions is less constrained and could cause a sizeable impact on observables. Therefore, a search for QBH production that violates SM global symmetries provides a possible way to examine low-scale gravity phenomena.

In the absence of coherent and reliable Feynman diagram technique for the quantum black hole description, the easiest and most accurate way to visualize the QBH production mechanism would be a set of partonic 2-to-2 scattering processes

$$uu \to \bar{d}\ell^{+}, \quad ud \to \bar{u}\ell^{+}, \quad d\bar{d} \to d\ell^{+}, \tag{1}$$

and the respective charge conjugates. Only these six electric charge initial-states (±4/3, ±2/3, ±1/3) can result in a lepton-quark or lepton-antiquark pair in the final-state. Here, the u and d symbols denote all up and down quark flavors and ℓ – all charged leptons excluding τ-lepton. In this way, all quark flavors are possible in both the initial and the final state in Eq. (1).

A previous search for QBHs in the lepton+jet channel was performed in proton-proton (pp) collisions at a center-of-mass energy of $\sqrt{s}$ = 8 TeV by ATLAS [12]. The combined 95% confidence level upper limit on the QBHs production cross-section with threshold mass above 3.5 TeV was found to be 0.18

fb. This limit constrains the threshold mass of QBH, which was found to be above 5.3 TeV in the ADD model. QBHs have also been sought in the dijet, dilepton, and photon-jet channels by both ATLAS and CMS at center-of-mass energies of 7 TeV [13–15], 8 TeV [16–20], and 13 TeV [21–25]. In general, the QBH searches in the lepton+jet final-state are less sensitive than in the dijet searches (at the same QBH threshold mass). On the other hand, the limits obtained in the lepton+jet events are stronger than those with photon+jet and dilepton final states.

2 ATLAS detector

The ATLAS experiment [26] at the LHC is a multipurpose particle detector with a forward–backward symmetric cylindrical geometry and a nearly 4π coverage in solid angle.[1] It consists of an inner tracking detector surrounded by a thin superconducting solenoid providing a 2 T axial magnetic field, electromagnetic and hadron calorimeters, and a muon spectrometer. The inner tracking detector covers the pseudorapidity range $|\eta| < 2.5$. It consists of silicon pixel [27], silicon microstrip, and transition radiation tracking detectors. Lead/liquid-argon (LAr) sampling calorimeters provide electromagnetic (EM) energy measurements with high granularity. A steel/scintillator-tile hadron calorimeter covers the central pseudorapidity range ($|\eta| < 1.7$). The endcap and forward regions are instrumented with LAr calorimeters for both the EM and hadronic energy measurements up to $|\eta| = 4.9$. The muon spectrometer surrounds the calorimeters and is based on three large superconducting air-core toroidal magnets with eight coils each. The field integral of the toroids ranges between 2.0 and 6.0 T m across most of the detector. The muon spectrometer includes a system of precision tracking chambers and fast detectors for triggering. A two-level trigger system [28] is used to select events. The first-level trigger is implemented in hardware and uses a subset of the detector information to accept events at a rate below 100 kHz. This is followed by a software-based trigger that reduces the accepted event rate to 1 kHz on average depending on the data-taking conditions. An extensive software suite [29] is used in data simulation, in the reconstruction and analysis of real and simulated data, in detector operations, and in the trigger and data acquisition systems of the experiment.

3 Data sets and simulated event samples

The results described in this paper use pp collision data collected by ATLAS at $\sqrt{s} = 13$ TeV during 2015–2018 in stable beam conditions and with all detector systems operating normally [30]. The event quality is checked to remove events with noise bursts or coherent noise in the calorimeters. Events in the electron channel are required to pass at least one of two single-electron triggers [31]: the first requires a transverse momentum (p_{T}) threshold of 60 GeV and the second has looser identification criteria and a p_{T} threshold of 120 or 140 GeV, depending on the data-taking period. Events in the muon channel are recorded using a single-muon trigger [32] with the transverse momentum (p_{T}) requirement of at least 50 GeV. The integrated luminosity of the dataset is determined to be $140.1 \pm 1.2\ \mathrm{fb}^{-1}$ [33], obtained using the LUCID-2 detector [34] for the primary luminosity measurements.

[1] ATLAS uses a right-handed coordinate system with its origin at the nominal interaction point (IP) in the centre of the detector and the z-axis along the beam pipe. The x-axis points from the IP to the centre of the LHC ring, and the y-axis points upwards. Cylindrical coordinates (r, ϕ) are used in the transverse plane, ϕ being the azimuthal angle around the z-axis. The pseudorapidity is defined in terms of the polar angle θ as $\eta = -\ln\tan(\theta/2)$. Angular distance is measured in units of $\Delta R \equiv \sqrt{(\Delta\eta)^2 + (\Delta\phi)^2}$.

Background events with a high-p_T lepton and one or more jets arise from electroweak processes including vector boson production with additional jets (W/Z+jets), dibosons (WW, WZ and ZZ), top-quark pair ($t\bar{t}$) and single-top-quark production, and multi-jet processes including non-prompt leptons from leptonic hadron decays and jets misidentified as leptons.

Monte Carlo (MC) simulation is used to model the expected contributions of various SM processes as well as possible QBH signals. A full description of the MC simulated event samples used is given below and summarized in Table 1. The expected contributions of the SM backgrounds reported in Table 1 are taken from MC simulation, either directly or after normalization to data in dedicated control regions. The multi-jet background is measured directly in data. Here, the events collected by a set of unprescaled single-lepton triggers with different p_T-thresholds are used.

W/Z+jets and diboson samples [35, 36] are simulated with the Sherpa generator [37]. The W/Z+jets, and semileptonically decaying diboson samples, are simulated with Sherpa 2.2.1, while the fully leptonic diboson processes are simulated with Sherpa 2.2.2. In the Sherpa samples the additional hard parton emissions [38] are matched to parton showers based on Catani–Seymour dipole factorization [39]. The `NNPDF3.0nlo` [40] set of parton distribution functions (PDFs) and a dedicated set of tuned parameters developed by the Sherpa authors are used [37]. The matching of the matrix element to the parton shower [41–44] is employed for the various jet multiplicities, which are then merged into an inclusive sample using an improved CKKW matching procedure [43] that is extended to next-to-leading-order (NLO) accuracy using the MEPS@NLO prescription [42]. The virtual QCD correction for matrix elements at NLO accuracy is provided by the OpenLoops library [45, 46]. The W/Z+jets (diboson) simulations are calculated for up to two (one) additional partons at NLO and up to four (three) additional partons at LO. The W/Z+jets processes are normalized to a next-to-next-to-leading-order (NNLO) cross-section prediction [47]. The diboson processes are normalized to the NNLO cross-section prediction [48] as well.

The production of $t\bar{t}$ [49] and single-top tW [50] and s-channel [51] events is modeled using the Powheg Box [52–54] v2 generator at NLO with the `NNPDF3.0nlo` PDF set. The single-top t-channel [55] is modeled with Powheg Box in the four-flavor scheme with the `NNPDF3.04fNLO` PDF set. The events are interfaced with Pythia 8.230 [56] using the A14 tune [57] and the `NNPDF2.3lo` PDF set [58]. The h_{damp} parameter[2] is set to 1.5 times the top-quark mass [59]. The $t\bar{t}$ inclusive production cross-section is corrected to the theory prediction at NNLO in QCD, including the resummation of next-to-next-to-leading logarithmic (NNLL) soft-gluon terms calculated using Top++2.0 [60]. The tW inclusive cross-section is corrected to the theory prediction calculated at NLO in QCD with NNLL soft-gluon corrections [61, 62]. The MadSpin [63] generator is used to preserve top-quark spin correlations in t-channel of the single top background. The EvtGen [64] package is applied for the modeling of c- and b-hadron decays.

The simulated QBH signal event samples are obtained from the QBH 3.0 generator [65], which uses the CTEQ6L1 leading-order PDF set [57, 66]. The parton showering and hadronization is performed in Pythia 8.205, using the CTEQ6L1 PDF set and the A14 tune. The QCD factorization scale for the PDFs is set to the inverse gravitational radius [65]. The equality of M_{th} and M_{D} is imposed for simplicity. The QBH mass is required to be below $3M_{\mathrm{D}}$ to avoid a region of possible thermal decays. For ADD QBH signal samples the number of extra dimensions is set to $n = 6$ (total number of dimensions $D = 10$). For RS1 QBH signal samples a single extra dimension is assumed, leading to a total of five dimensions. The ADD (RS1) samples for both leptonic channels are generated with M_{th} from 2 TeV to 9.5 (7.5) TeV with steps of

[2] The h_{damp} parameter controls the p_T of the first additional emission beyond the leading-order Feynman diagram in the parton shower and therefore regulates the high-p_T emission against which the $t\bar{t}$ system recoils.

Table 1: The event generators used for simulation of the signal and background processes. The acronyms ME and PS stand for Matrix Element and Parton Shower. The top-quark mass is set to 172.5 GeV.

Process	ME Generator and ME PDFs	PS, PDFs, non-perturbative effect
W/Z+jets	Sherpa 2.2.1, `NNPDF3.0nlo`	Sherpa 2.2.1, `NNPDF3.0nlo`
$t\bar{t}$	Powheg Box, `NNPDF3.0nlo`	Pythia 8.230, `NNPDF2.3lo`, EvtGen1.6.0
Single top s-channel, tW	Powheg Box, `NNPDF3.0nlo`	Pythia 8.230, `NNPDF2.3lo`, EvtGen1.6.0
Single top t-channel	Powheg Box, `NNPDF3.04fNLO`, MadSpin	Pythia 8.230, `NNPDF2.3lo`, EvtGen1.6.0
Diboson, semi-leptonic decay	Sherpa 2.2.1, `NNPDF3.0nlo`	Sherpa 2.2.1, `NNPDF3.0nlo`
Diboson, fully leptonic decay	Sherpa 2.2.2, `NNPDF3.0nlo`	Sherpa 2.2.2, `NNPDF3.0nlo`
QBH signal, ADD, RS1	QBH 3.0, CTEQ6L1	Pythia 8.205, CTEQ6L1, EvtGen1.2.0

0.5 TeV (the same as in Ref. [12]). A quantum black hole is not a particle, so it does not have a single mass or width. It is produced with a mass distribution. The generator produces a distribution of QBH masses (with no additional mass smearing). The decay products have exactly the energy and momentum of the produced black hole. Unlike particles produced in quantum field theory, the black hole is produced in a non-perturbative gravity model. The cross-sections predicted by the QBH 3.0 event generator [65] are used in the determination of the model-dependent limits for the signal processes. Processes with a quark pair in the initial state have at least two orders of magnitude higher cross-sections than those with antiquark pairs in the initial state.

All simulated event samples include the effect of multiple pp interactions in the same or neighboring bunch crossings. These effects are collectively referred to as pile-up. The simulation of pile-up collisions is performed with Pythia 8.186 using the ATLAS A3 set of tuned parameters [67] and the `NNPDF2.3lo` PDF set and weighted to reproduce the average number of pile-up interactions per bunch crossing observed in data. The generated background events are passed through a full detector simulation [68] based on Geant4 [69]. Simulated QBH event samples are produced with a fast parametrization of the calorimeter response [70], while Geant4 is used for the other detector systems.

4 Event reconstruction and object identification

For an event to be considered, at least one pp interaction vertex with at least two tracks must be reconstructed. The primary vertex is chosen to be the vertex with the highest summed p_{T}^2 of tracks with transverse momentum $p_{\mathrm{T}} > 0.4$ GeV that are associated with the vertex [71].

Two identification levels are defined for leptons and jets, referred to as "Baseline" and "Signal," with Signal objects being a subset of Baseline. The Baseline leptons are required to satisfy Loose [72] identification and isolation criteria. Baseline jets are required to have $p_{\mathrm{T}} > 20$ GeV which is less than the value for Signal jets. This requirement provides a higher selection efficiency for leptons and jets when calculating missing transverse momentum and resolving ambiguities between overlapping physics objects (see below in this Section).

Electron candidates are reconstructed using energy clusters in the EM calorimeter which are matched to an ID track, and they are calibrated as described in Ref. [72]. Baseline electron candidates are required to have $|\eta| < 2.47$ in order to pass through the fine-granularity region of the EM calorimeter and be outside the range $1.37 < |\eta| < 1.52$ corresponding to the transition region between the barrel and endcap EM calorimeters. They should also satisfy Loose identification criteria and have $p_{\mathrm{T}} > 10$ GeV. The trajectory of Baseline electrons must be consistent with the primary vertex to suppress electrons originating from pile-up. Therefore, the tracks associated with BASELINE electrons must have a longitudinal impact parameter relative to the primary vertex (z_0) such that $|z_0 \sin\theta| < 0.5$ mm. SIGNAL electrons are defined as BASELINE candidates that have $p_{\mathrm{T}} > 30$ GeV and satisfy the TIGHT identification and HIGHPTCALOONLY isolation requirements [72]. The track associated with each SIGNAL electron must have a transverse impact parameter significance $|d_0/\sigma(d_0)| \leq 5$.

BASELINE muon candidates are reconstructed in the region $|\eta| < 2.7$ by matching ID tracks to tracks reconstructed in the MS, and they are calibrated in situ using $Z \to \mu\mu$ decays [73]. BASELINE muon candidates are required to have $p_{\mathrm{T}} > 10$ GeV. They have to satisfy a set of requirements on the quality of the tracks defined as MEDIUM [73] and to pass an impact parameter cut of $|z_0 \sin\theta| < 0.5$ mm. SIGNAL muons are defined as BASELINE candidates that have $p_{\mathrm{T}} > 30$ GeV, pass a requirement on significance of transverse impact parameter $|d_0/\sigma(d_0)| \leq 3$, and satisfy HIGHPT muon identification requirements [73] and a track-based isolation criterion. For the isolation requirement, the summed p_{T} of tracks originating from the primary vertex within a cone of radius $\Delta R = 0.2$ around the muon, but excluding the muon-candidate track itself, has to be less than 1.25 GeV. A bad-muon veto for the HIGHPT muons is applied. An event is rejected when a muon has a large relative error of charge over momentum (q/p) associated with the track. The veto efficiency depends on p_{T} and η.

The anti-k_t algorithm [74] with distance parameter $R = 0.4$ implemented in the `FastJet` library [75] is used to reconstruct jets up to $|\eta| = 4.9$ from massless clusters of energy depositions in the calorimeter [76] (EMTopo jets). Jets are then calibrated as described in Ref. [77, 78]. BASELINE jets are required to have $p_{\mathrm{T}} > 20$ GeV and $|\eta| < 2.8$. Events are vetoed if they contain jets induced by calorimeter noise or non-collision background, according to criteria described in Ref. [79]. Additional jets that arise from pile-up interactions are rejected by applying a dedicated track-based selection (Jet Vertex Tagger [80]), based on classifying the tracks associated with the jet as pointing or not pointing to the primary vertex. The jet candidates passing all the above requirements are called BASELINE jets. SIGNAL jets are defined as BASELINE candidates that have $p_{\mathrm{T}} > 30$ GeV.

Jets containing b-flavored hadrons, used only for estimation of some backgrounds, are identified in the region $|\eta| < 2.5$ by the MV2c10 algorithm [81], which makes use of the impact parameters of tracks associated with the candidate jet, the positions of reconstructed secondary vertices and their consistency with the decay chains of such hadrons. For the working point chosen for this analysis, such jets are identified with an average efficiency of 77% in simulated $t\bar{t}$ events [82], corresponding to rejection factors of 110, 4.9 and 15 for jets originating from light quarks or gluons, charm quarks and τ leptons, respectively.

To avoid reconstruction of a single detected object as multiple leptons or jets, an overlap removal procedure is applied to BASELINE leptons and jets. First, jet candidates are discarded if they are within $\Delta R < 0.2$ of an electron. Second, electron candidates are discarded within $\Delta R < 0.4$ of the remaining jets. Finally, muon candidates are discarded if they are within $\Delta R < 0.4$ of a remaining jet with at least three tracks of $p_{\mathrm{T}} > 500$ MeV; if this jet has less than three tracks, it is discarded and the muon is kept instead.

The missing transverse momentum (whose magnitude is denoted $E_{\mathrm{T}}^{\mathrm{miss}}$) is defined as the negative vector sum of the transverse momenta of all identified objects (BASELINE electrons, photons, muons, jets and τ-leptons) and an additional soft term. The overlap removal between baseline objects is applied before computing $E_{\mathrm{T}}^{\mathrm{miss}}$. The soft term is constructed from all tracks associated with the primary vertex but not with any physics object. Fully calibrated electrons, muons, photons, jets, hadronically decaying τ-leptons and charged-particle tracks are used to reconstruct $E_{\mathrm{T}}^{\mathrm{miss}}$ [83, 84].

5 Event selection and background estimation strategy

The event selection is designed to be efficient for true electron+jet and muon+jet final states. For candidate signal events, $p_T > 130$ GeV is required for both the highest p_T (leading) lepton and the highest p_T jet. The invariant mass of this lepton+jet pair, m_{inv}, is required to be greater than 2.0 TeV in the signal region. A veto on subleading leptons with $p_T > 10$ GeV is applied. A requirement that the $p_T < 130$ GeV is applied on subleading jets in the event. These selection requirements are summarized in Table 2.

Acceptance and efficiency are estimated with the use of the simulated QBH signal event samples. Acceptance is the fraction of events passing the true Signal requirements with true kinematic variables at the generator level. Efficiency is the fraction of events passing the Signal requirements after reconstruction with respect to the true Signal requirements. The product of acceptance and efficiency ($Acc \times Eff$) of the signal selection is equal to $(66.5 \pm 0.4)\%$ and $(67.1 \pm 0.4)\%$ in the electron and muon channels, respectively. These values do not depend on the QBH threshold mass (M_{th}) within their uncertainties. The $Acc \times Eff$ is consistent for both models (ADD and RS1) at the same value of M_{th}.

The dominant background in both channels is the W+jets process in which the W boson decays leptonically. In the electron+jet channel, the second largest background is events with non-prompt and fake leptons. It mostly originates from multi-jet production processes when one of the jets is misidentified as a lepton. This background source adds less than seven events in the SR, for the muon channel. Its contribution is four times smaller than the single-top background and ten times smaller than the total uncertainty on the sum of all the other background contributions in the SR: it is therefore considered to be negligible in the muon+jet channel. There are also contributions from the Z+jets events in which one lepton is not detected; from diboson processes in which at least one boson decays leptonically; as well as from $t\bar{t}$ and single-top-quark production, in which the W boson from the top-quark decays leptonically.

The background yields for W/Z+jets and $t\bar{t}$ processes in the signal region (SR) are estimated using dedicated control regions (CRs) and confirmed in validation regions (VRs). The control (validation) regions enriched with W/Z+jets and $t\bar{t}$ backgrounds are designated as WCR (WVR), ZCR (ZVR) and TCR (TVR), respectively. They are orthogonal to each other. There are different CRs and VRs in the electron+jet and muon+jet channels. Definitions of all regions are given in Table 2. The CRs/VRs are defined using m_{inv} requirements and additional cuts to increase the purity of the corresponding background (last 3 rows in Table 2). The signal contamination estimated for the CRs is less than 0.3% for the ADD signal with $M_{th} = 5$ TeV. This M_{th} value is considered since lower masses were excluded by the previous analysis at 8 TeV [12]. An additional validation region, SVR, is used to verify the agreement of background with data in the phase space that is close to the SR. The SVR uses the same selections as the SR but with lower m_{inv} (see Table 2).

The multi-jet background for the electron channel is estimated using the data-driven *Matrix Method* described in Ref. [85]. Two parameters of the method (real and fake efficiencies, r and f) are evaluated using the MC simulated samples of the W/Z+jets background and the data samples. Events in the samples are selected with looser object requirements with respect to the Baseline selection to enrich the selected events with non-prompt electrons and non-electron objects identified as electrons. The *Matrix Method* uses *tight* and *loose* selection. The *tight* selection corresponds to the Signal requirement. In contrast to *tight*, the *loose* selection uses the Loose identification and does not apply the isolation requirement. The r value is the fraction of the electron candidates passing the *tight* requirements and matched to a generated electron, with respect to the electron candidates passing *loose* selection and matched also to a generated electron. The f value is the fraction of the electron candidates passing the *tight* requirements,

Table 2: Definitions of the control, validation and signal regions. Note, that "–" means that this criterion is not applied. Two same-flavor opposite-sign (SFOS) leptons satisfying the Signal selection criteria are required in the Z+jets control and validation regions; while Signal and Baseline stand for the corresponding sets of the lepton and jet selection criteria.

Event selection	WCR (WVR)	ZCR (ZVR)	TCR (TVR)	SR (SVR)
m_{inv} [TeV]	1.0–1.5 (1.5–2.0)	1.0–1.5 (1.5–2.0)	1.0–1.5 (1.5–2.0)	>2.0 (1.5–2.0)
Leading lepton, p_{T} [GeV]	Signal, >130	Signal, >130	Signal, >130	Signal, >130
Subleading leptons, p_{T} [GeV]	Baseline, <10	SFOS, >30	Baseline, <10	Baseline, <10
Leading jet, p_{T} [GeV]	Signal, >130	Signal, >130	Signal, >130	Signal, >130
Subleading jets, p_{T} [GeV]	Signal, <130	Signal, <130	Signal, <130, N≥3	Signal, <130
Number of b-tagged jets	0	–	≥2	–
$E_{\text{T}}^{\text{miss}}$ [GeV]	>60	–	–	–
$m_{\ell^+\ell^-}$ [GeV]	–	70–110	–	–

but not matched to any generated electron (fake), with respect to the candidate electrons passing the *loose* selection and not matched to any generated electron. The r and f efficiencies and their uncertainties are estimated as function of lepton p_{T} and η, and they cover all regions. The r and f efficiencies are a part of the fake/non-prompt lepton backgrounds estimation toolset [86] that is developed using data and MC simulations and is validated in data. Estimation of the r and f uncertainties is described in Section 7. The number of events with fake electrons (N_{multijet}) selected with the *tight* requirement is estimated as

$$N_{\text{multijet}} = \frac{f}{r-f}(r(N_l + N_t) - N_t), \tag{2}$$

where N_t is the total number of electron candidates passing the *tight* selection in the data sample. N_l is the number of electron candidates that pass the *loose* selection and fail the *tight* requirements in the data.

All background processes except the multi-jet background are estimated using MC simulated events. The control regions are used to constrain the freely floating W+jets, Z+jets and $t\bar{t}$ background normalization factors, which are obtained independently for the electron+jet and muon+jet channels. The normalizations for the multi-jet, diboson and single top backgrounds are allowed to vary, but only within their uncertainty ranges. The systematic uncertainties on the expected event yields are included as nuisance parameters and are assumed to follow Gaussian distributions with width determined from the size of the corresponding uncertainty. The fit parameters are determined by maximizing the product of the Poisson probability functions and the constraints on the nuisance parameters.

6 Statistical analysis

A QBH signal is sought in the m_{inv} distributions in the electron+jet and muon+jet channels as well as in their combination. The statistical interpretation of the results is performed using the profile likelihood method implemented in the HistFitter framework [87]. The likelihood function is a product of the probability density functions of the binned m_{inv} distributions, with one for each region contributing to the fit. The number of events in each of the bins in the given regions is described using a Poisson distribution, the mean of which is the sum of the expected contributions from all background and signal sources. Systematic uncertainties described in Section 7 are added into the fit as nuisance parameters. Normalization factors are free-floating parameters in the fit. The combination of the electron and muon channels was made by merging the electron and muon samples in the data and in the MC. The sum of the MC events takes into account weights related to efficiency of trigger, reconstruction, identification, isolation, pile-up, etc. The combined channel (lepton+jet) is fitted independently for the electron and muon channels. Two types of fits are performed as detailed below.

A *model-independent* fit compares the data event yield in the SR with the SM background estimate and its uncertainties, to test for possible contribution of any non-SM signal in the SR. As a first step, a *background-only* fit is performed, where the normalization and shape-fit of the backgrounds is adjusted to match the data in the three control regions simultaneously. The resulting distributions are extrapolated into the signal region to correct the expected shapes and yields of the corresponding backgrounds. The extrapolation of the adjusted distributions and nuisance parameters is also checked in the VRs by means of comparison to data and total yield of the SM background. In a second step, any non-SM signal is sought in the SR. The possible contribution of a signal is scaled by a freely floating normalization factor of the dummy signal added in the SR. The significance of a possible excess of observed events over the SM prediction is quantified by the one-sided probability, p_0, of the background alone to fluctuate to the observed number of events or higher, by using the asymptotic formula described in Ref. [88]. The presence of a non-SM signal would manifest itself in a small p_0 value. In the absence of an excess over the SM expectation, upper limits on the cross-section of any non-SM signal are estimated.

In a *model-dependent* fit, an ADD or RS1 signal is added to the SR, and its yield is scaled by a freely floating signal normalization factor. In the absence of any significant excess above the SM background prediction, limits are evaluated with the modified frequentist $\mathrm{CL_S}$ method [89] using pseudo-experiments. The background normalization factors and nuisance parameters are determined simultaneously in the CRs and in the SR. The bin width in the SR is optimized to obtain good fit performance and stability for all QBH masses in the range 2–9.5 TeV. The 2 TeV width was found to be the best bin size.

7 Systematic uncertainties

Systematic uncertainties are evaluated for all signal and background predictions and include experimental uncertainties on detector measurements as well as modeling uncertainties and the effect of limited statistics of MC simulation. The systematic uncertainties of all backgrounds are extrapolated from the control regions into the validation and signal regions in the background-only fit. The expected QBH signal and its uncertainties are estimated for the ADD and RS1 models in the model-dependent fit. The relative systematic uncertainties for the SM background and signal (ADD, M_{th} = 6.0 TeV) in the SR are represented in Table 3. The resulting uncertainty in the total background differs from the sum in quadrature of the single sources because of correlations.

Experimental uncertainties reflect the accuracy of the experimental measurements of jets and leptons. The jet energy scale (JES) and resolution (JER) uncertainties are derived as a function of the p_{T} and η of the jet. They are determined using a combination of data and simulation, through measurements of the jet p_{T} balance in dijet, Z+jets and γ+jets events [78]. The uncertainties in scale and resolution of the electron energy [72] and muon momentum [73] are propagated to the measured event yield. Systematic uncertainties in the measurements of the electron [31, 72] and muon [73] identification, reconstruction, isolation, and triggering efficiencies as well as in the pile-up jet identification using the jet vertex tagger algorithm [80] are also propagated to the measured m_{inv} distributions.

Table 3: The relative systematic uncertainties (in %) on the SM background in the SR are estimated in the background-only fit; and systematic uncertainties on the ADD signal are estimated for the QBH with $M_{\text{th}} = 6.0$ TeV in the model-dependent fit. Lepton modeling combines all the types of experimental uncertainties for the electrons or muons. All the uncertainties shown are obtained independently for the electron and muon channels. The relative statistical errors on the data (in %) are also shown.

Source	Electron+jet		Muon+jet	
	Background	Signal	Background	Signal
JER	2.4	1.9	2.4	1.6
JES	0.7	0.4	0.6	0.5
Lepton modeling	2.8	0.6	3.6	1.7
Pile-up	0.7	0.6	0.8	1.0
Luminosity	0.5	0.7	0.5	0.7
W+jets normalization	1.1	–	1.1	–
W+jets modeling	0.5	–	0.6	–
Z+jets normalization	0.3	–	0.3	–
Z+jets modeling	0.3	–	0.3	–
$t\bar{t}$ normalization	0.2	–	0.4	–
MC statistics	1.6	0.6	1.5	0.7
Multi-jet estimation	1.4	–	–	–
Total uncertainty	4.6	2.4	5.1	2.7
Statistical errors of data	2.1	–	2.7	–

The uncertainty in the m_{inv} spectrum due to pile-up is estimated by varying the average number of pile-up events in the simulation to account for the differences between the values of the measured and predicted total inelastic cross-section used in the pile-up simulation [90]. The impact of the luminosity uncertainty on the SM background is estimated by varying the integrated luminosity combined over 2015–2018 within its uncertainty of 0.83% [33].

Modeling uncertainties on the W/Z+jets backgrounds are calculated as follows. The PDF uncertainties propagated to the m_{inv} distribution are estimated using the nominal PDF set and a set of 100 PDF replicas for `NNPDF3.0nnlo` [40]. The impact of the $\alpha_s(m_Z)$ uncertainty on the background is estimated by varying $\Delta\alpha_s(m_Z) = \pm 0.002$. The impact of missing higher order calculations is evaluated using seven-point variations of the factorization and renormalization scales in the cross-section calculations. The scales are independently varied upwards and downwards by a factor of two, excluding simultaneous variations in opposite directions. The envelope of the resulting variations as a function of m_{inv} is taken as the size of the associated systematic uncertainty. All aforementioned modeling uncertainties are combined in quadrature and represented in Table 3 as "W/Z+jets modeling." Total modeling (theoretical) uncertainties are not estimated for the $t\bar{t}$, single-top and diboson samples because they are small backgrounds. The uncertainties in the normalization of the W/Z+jets and $t\bar{t}$ backgrounds from the fitting procedure are shown in Table 3 as well as uncertainties from the limited MC statistics of the background simulated samples.

The uncertainties in the multi-jet background are related to the estimate of the f and r parameters (Δf and Δr) as well as to statistical errors in the total number N_t of *tight* electron candidates (ΔN_t) and in the total number N_l of *loose* electron candidates (ΔN_l). The Δf and Δr uncertainties are estimated for different ($\eta - p_{\text{T}}$) regions by varying the requirements used in the event selection [85]. All these uncertainties are combined in quadrature and reported in Table 3.

Systematic uncertainties described in this section are added into the fit as nuisance parameters where they can be pulled and constrained. After the fit all systematic uncertainties are found to be pulled by less than 0.7 of their amplitude. The errors of nuisance parameters are constrained within $\pm 0.5\sigma$ in comparison with their initial values.

8 Results

In the *background-only* fit, the normalization factors of the W+jets, Z+jets and $t\bar{t}$ background processes are consistent with unity within uncertainties. Differences of normalization factors from unity are $\leq$5% in all cases. The m_{inv} distributions of events in the WCR, ZCR, TCR and corresponding validation regions after the *background-only* fit are shown in Fig. 1. There is good agreement between the data and the SM background in all CRs and VRs.

The comparison of the post-fit background yields with the data in the SVR and SR is represented in Table 4. The pre-fit background yields expected in the MC are shown in the bottom part of Table 4. There is agreement between the data ("Observed data") and the total SM background ("Fitted events") within 1σ in all regions. The errors include both statistical and systematic uncertainties. The pre-fit W+jet background in the electron channel has a visible slope when compared to data. The deviation exceeds the total uncertainty, and the difference reaches 7% at high m_{inv} even in the WCR. In the WVR it increases from 8% to ~20% with m_{inv}. The difference reaches ~10% (20%) in the SVR (SR). The likelihood shape-fit used in the analysis eliminates the slope and attains agreement between background and data within their uncertainties. Therefore, the difference between the pre-fit and post-fit yields for W+jet background in Table 4 is related to the slope adjustment rather than to the normalization that is certain to be the same in all regions. The change in the background slope provides a 22% decrease in the W+jet yields in the electron SR. The pull values are mainly related to nuisance parameters (uncertainties on objects, detector, and modeling), rather than to slope elimination. The pull of the uncertainty on the W+jet background in the SR of the electron channel, in Table 4, is equal to $(70 - 65)/65 = 0.08$. The pull of the uncertainty on the total background is equal to $(110 - 94)/94 = 0.17$.

The m_{inv} distributions after the *background-only* fit shown in Fig. 2 have good agreement between the data and the SM background in the SR in both the electron+jet and the muon+jet channels. The differences between the data and background are within 1σ. The highest invariant mass of a lepton+jet pair reconstructed in the electron (muon) channel is 4.74 TeV (4.96 TeV).

The *model-independent* fit is performed simultaneously in the WCR, ZCR, TCR and a single-bin SR to test for a non-SM signal contribution. The possible contribution of signal events is scaled by a freely floating signal normalization factor. No significant excess above the SM background prediction is observed in either of the channels. The *model-independent* upper limit on the cross-section times branching fraction ($\sigma \times Br$) is estimated with pseudo-experiments at 95% confidence level (C.L.) for the production of a non-SM signal. Figure 3 shows the upper limits on the $\sigma \times Br$ (circles along the solid red line) integrated above the lower threshold of the SR (events with $m_{inv} > \mathrm{Th}_{\mathrm{SR}}$) for the lepton+jet channel (combined channel of electron+jet and muon+jet).

In the *model-dependent* fit, the 5-bin m_{inv} distributions of signal and backgrounds in the SR are fitted simultaneously with background in three CRs. The number of ADD (RS1) signal events is scaled by a freely floating signal normalization factor. The background normalization factors are also determined simultaneously in the fit in the CRs, and they are consistent with those of the *background-only* fit. There

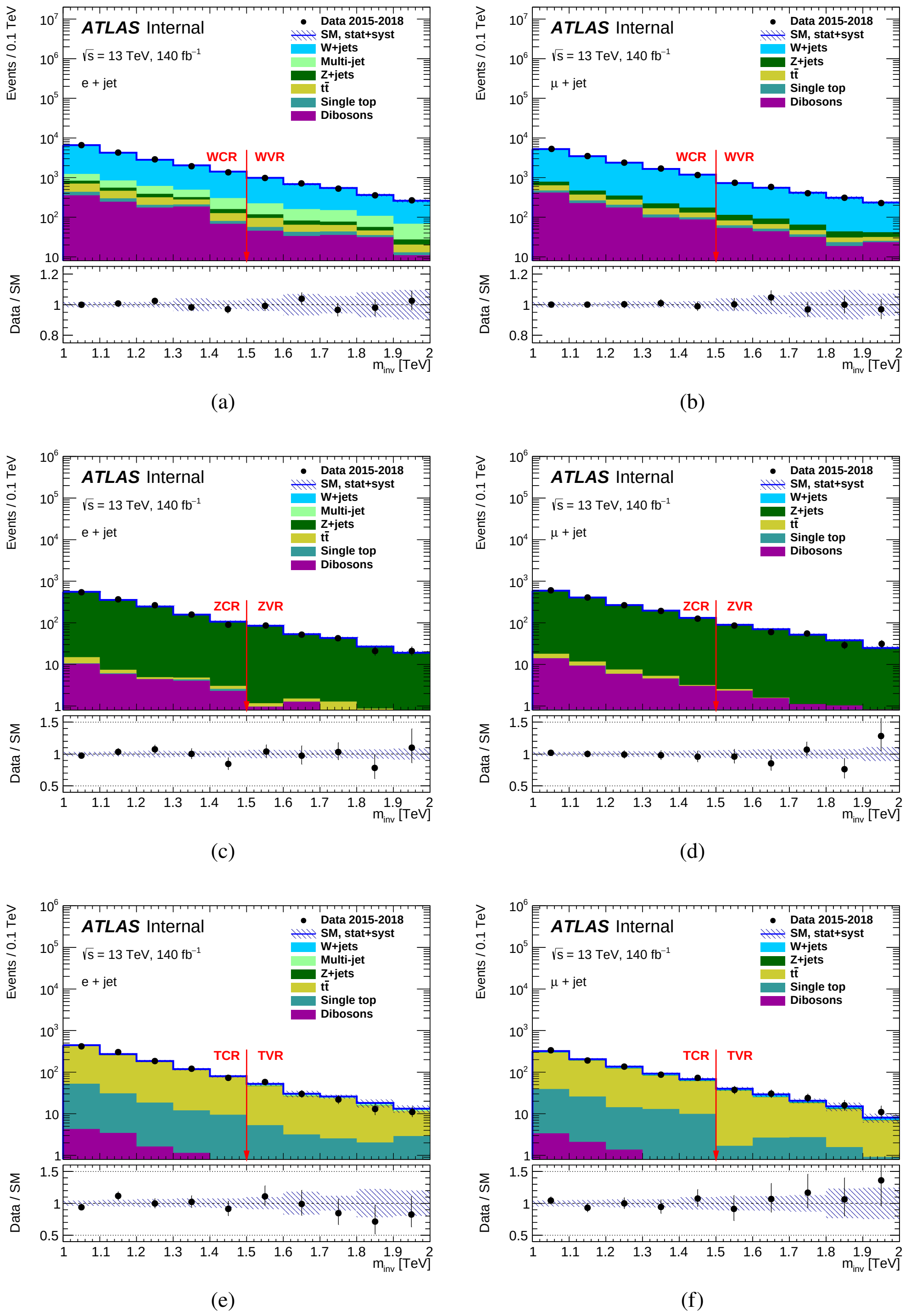

Figure 1: The distributions of events over the invariant mass of the leading lepton and the leading jet are shown after the *background-only* fit. The data (points with error bars) and SM backgrounds (solid histograms) are shown in (a, c, e) for the electron+jet channel and in (b, d, f) for the muon+jet channel. The normalizations extracted from the fit in the CRs are applied in the full m_{inv} range. (a, b) show the WCR and WVR; (c, d) the ZCR and ZVR; and (e, f) the TCR and TVR. The lower panels show the ratio of the number of events observed in the data to the fitted total background. The hatched bands represent the total relative uncertainty in the background estimate.

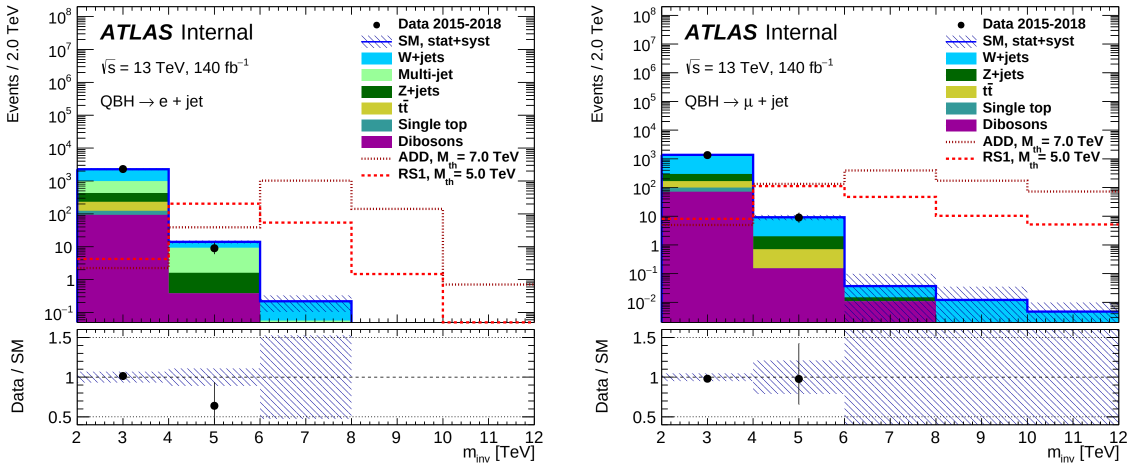

(a) (b)

Figure 2: The distributions of events over the invariant mass of the leading lepton and the leading jet in the SR for data (points with error bars) and for SM backgrounds (solid histograms) after the *background-only* fit are shown in: (a) the electron+jet and (b) the muon+jet channels. The normalizations extracted from the fit in the CRs are applied in the full m_{inv} range including the SR. The sum of the systematic uncertainties and the statistical errors due to the limited size of the fitted MC samples is shown by the hatched area. The lower panels show the ratios of the number of events observed in the data to the fitted total background. The hatched band represents the total relative uncertainty in the background estimate. Two examples of QBH signals normalized to the predicted cross-section are overlaid.

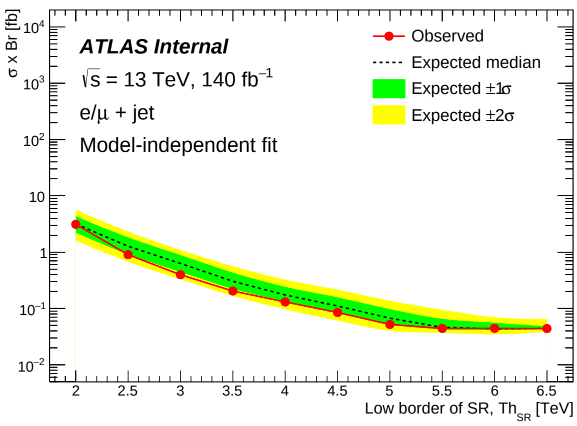

Figure 3: The 95% C.L. *model-independent* upper limits on $\sigma \times Br$ for the non-SM signal production with decay into the lepton+jet (combined channel). The limits take into account statistical and systematic uncertainties. Circles along the solid red line indicate the lower border of the SR (threshold of SR, Th_{SR}), above which the observed limit is computed. The expected limits are shown by the dashed line. The $\pm 1\sigma$ and $\pm 2\sigma$ bands of expected limits are shown in green and yellow, respectively. The limits are obtained with pseudo-experiments.

Table 4: The observed number of data events, the fitted background events in the SVR and the SR for the *background-only* fit and the number of background events expected from the MC background samples in the electron+jet and muon+jet channels. The errors shown for the "Expected events" are statistical and systematic uncertainties summed in quadrature.

	SVR electron+jet	SVR muon+jet	SR electron+jet	SR muon+jet
Observed data	9053	5504	2319	1359
Fitted events	8900 ± 320	5380 ± 200	2290 ± 110	1386 ± 70
W+jets	5590 ± 270	4190 ± 200	1290 ± 70	1087 ± 54
Multi-jet	1670 ± 200	–	570 ± 47	–
Z+jets	646 ± 73	439 ± 27	199 ± 17	131 ± 13
$t\bar{t}$	527 ± 10	351 ± 7	109 ± 5	69 ± 5
Single top	143 ± 7	112 ± 5	31 ± 2	28 ± 2
Dibosons	335 ± 22	289 ± 14	94 ± 9	72 ± 8
Expected events	9390 ± 340	5260 ± 220	2647 ± 94	1303 ± 55
W+jets	6090 ± 270	4080 ± 210	1654 ± 65	1016 ± 48
Multi-jet	1690 ± 210	–	577 ± 38	–
Z+jets	598 ± 85	408 ± 23	186 ± 18	122 ± 12
$t\bar{t}$	546 ± 14	366 ± 7	109 ± 6	71 ± 5
Single top	141 ± 7	104 ± 4	29 ± 2	28 ± 2
Dibosons	327 ± 23	298 ± 12	92 ± 10	66 ± 8

is no evidence of a QBH signal at any M_{th} in both models. Figure 4 shows the 95% C.L. upper limit on the cross-section times branching fraction[3] ($\sigma \times Br$) as a function of M_{th} for the combined lepton+jet channel in the SR for the production of a QBH in the ADD and RS1 models. The limits are obtained with a spacing of 0.5 TeV in M_{th} and are linearly interpolated between the points. The limits are obtained using pseudo-experiments.

For a QBH decaying into a lepton+jet pair, the suppression of the additional jet activity in the event leads to a better separation between the signal and SM background production processes. However, the constraint of the subleading jet p_{T} to be less than 130 GeV distorts the acceptance and efficiency of the signal extraction, since the QBH signal is calculated at LO+PS accuracy in QCD, while the largest SM backgrounds, V+jets, are generated with NLO+PS precision. Thus, the comparison of signal with background may be distorted in the fit, leading to an over-optimistic estimate of the signal production cross-section. The effect of the higher order QCD radiation on the QBH production yield is estimated with a help of the correction factor R_c. R_c is obtained with the use of the W/Z+jets event samples that have a similar color structure in the final-state and are calculated at NLO+PS accuracy in QCD. R_c shows how much the signal acceptance is overestimated because of the use of the jet p_{T} constraint in a LO MC. The multiplication of R_c and cross-section obtained in the fit, σ_{fit}, effectively corrects the signal yield and the derived limits ($\sigma = R_c \times \sigma_{fit}$). This correction should give the same result as the multi-step correction process that was used, but it is more straightforward to understand.

R_c is defined as the ratio of the number of events passing the signal selection without and with the cut on the subleading jet activity (this cut is in Table 2). The ratios are calculated separately for W+jets and Z+jets events, and the average of the two is used as the R_c correction factor. The maximal difference

[3] There are six QBH states that can decay to lepton+jet. As each state has a different production cross-section and branching fraction, the limits set an effective limit which is a sum over all possible QBH states.

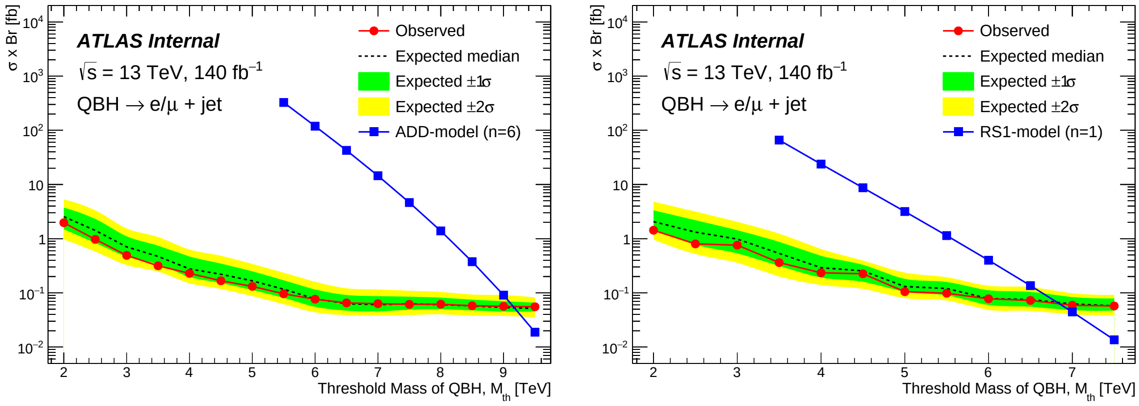

(a) (b)

Figure 4: The combined 95% C.L. upper limits on $\sigma \times Br$ as a function of M_{th} for QBH production at $M_{\text{th}} = M_{\text{D}}$ with decay into lepton+jet for (a) ADD (extra dimensions $n = 6$) and (b) RS1 (extra dimensions $n = 1$). The limits take into account statistical and systematic uncertainties. Circles along the solid red line indicate the mass M_{th} of the signal where the observed limit is computed. The expected limits are shown by the dashed line. The $\pm 1\sigma$ and $\pm 2\sigma$ bands are shown in green and yellow, respectively. The theoretically predicted $\sigma \times Br$ for the QBH production and decay is shown as the solid blue curve with squares.

between corrections obtained in the W+jets and Z+jets samples is used as the systematic uncertainty on the R_c factor. Statistical uncertainties in the W/Z+jets samples are also included in the R_c total uncertainty. The uncertainty on R_c was added to the total systematic uncertainty in the fit. The QCD correction for the electron-jet and muon-jet final-state combination is calculated as the weighted average R_c in each decay channel. The magnitudes of R_c with its errors for electrons, muons and the combination are given below:

$$\langle R_c \rangle^{\text{ele}} = 2.80 \pm 0.18, \quad \langle R_c \rangle^{\text{muo}} = 2.58 \pm 0.26, \quad \langle R_c \rangle^{\text{comb}} = 2.72 \pm 0.15. \tag{3}$$

The cross-section upper limits obtained with the fit are further scaled by the R_c factor to correct for missing higher order QCD radiations. The upper limit values reported in Figures 3 and 4 and Table 5 include the R_c correction.

The lower limits on M_{th} for ADD and RS1, upper limits on $\sigma \times Br$ at the M_{th} mass point limits and model-independent upper limits on $\sigma(m_{\text{inv}} > 5\ \text{TeV}) \times Br$ are shown in Table 5. Accounting for QCD radiation effects in the QBH production using the R_c correction factor leads to conservative limit estimates. Future QBH lepton+jet analyses have the potential to explore higher QBH mass ranges and lower QBH production cross-section values once hard QCD radiation effects are included in the QBH event generation model.

Table 5: The lower limits on M_{th} and the upper limits on $\sigma \times Br$ at these mass points for QBHs decaying to a lepton and jet in the ADD and RS1 models. The model-independent upper limits on $\sigma \times Br$ are shown at $m_{\text{inv}} > 5$ TeV.

Channel	ADD $\sigma \times Br$ [fb]	ADD M_{th} [TeV]	RS1 $\sigma \times Br$ [fb]	RS1 M_{th} [TeV]	Model-independent $\sigma(m_{\text{inv}} > 5\ \text{TeV}) \times Br$ [fb]
Electron+jet	0.091	9.0	0.099	6.6	0.095
Muon+jet	0.083	9.0	0.087	6.7	0.084
Combined	0.056	9.2	0.061	6.8	0.052

9 Conclusion

The ATLAS detector at the LHC has been used to search for new phenomena in the lepton+jet invariant mass spectrum. The search is performed with 140 fb^{-1} of proton–proton collision data at $\sqrt{s}$ = 13 TeV, recorded during 2015–2018. The observed invariant mass spectrum of lepton+jet pairs is consistent with SM expectations. Upper exclusion limits are set on the cross-section times branching fraction for quantum black holes decaying to a lepton and a quark in a search region with invariant mass above 2.0 TeV. The resulting lower mass threshold limits in the ADD (RS1) models with six (one) extra dimensions at the 95% C.L. are 9.2 (6.8) TeV. The obtained limits show a factor of 3.5 improvement with respect to the previous model-independent upper limit on $\sigma \times Br$ [12]. The obtained limit on the QBH threshold mass for the ADD model is 3.9 TeV higher compared to the previous ATLAS result at 8 TeV [12]. The obtained limit on the QBH M_{th} for the RS1 model is determined for the first time in the lepton+jet decay mode.

Acknowledgements

We thank CERN for the very successful operation of the LHC, as well as the support staff from our institutions without whom ATLAS could not be operated efficiently.

We acknowledge the support of ANPCyT, Argentina; YerPhI, Armenia; ARC, Australia; BMWFW and FWF, Austria; ANAS, Azerbaijan; CNPq and FAPESP, Brazil; NSERC, NRC and CFI, Canada; CERN; ANID, Chile; CAS, MOST and NSFC, China; Minciencias, Colombia; MEYS CR, Czech Republic; DNRF and DNSRC, Denmark; IN2P3-CNRS and CEA-DRF/IRFU, France; SRNSFG, Georgia; BMBF, HGF and MPG, Germany; GSRI, Greece; RGC and Hong Kong SAR, China; ISF and Benoziyo Center, Israel; INFN, Italy; MEXT and JSPS, Japan; CNRST, Morocco; NWO, Netherlands; RCN, Norway; MEiN, Poland; FCT, Portugal; MNE/IFA, Romania; MESTD, Serbia; MSSR, Slovakia; ARRS and MIZŠ, Slovenia; DSI/NRF, South Africa; MICINN, Spain; SRC and Wallenberg Foundation, Sweden; SERI, SNSF and Cantons of Bern and Geneva, Switzerland; MOST, Taiwan; TENMAK, Türkiye; STFC, United Kingdom; DOE and NSF, United States of America. In addition, individual groups and members have received support from BCKDF, CANARIE, Compute Canada and CRC, Canada; PRIMUS 21/SCI/017 and UNCE SCI/013, Czech Republic; COST, ERC, ERDF, Horizon 2020 and Marie Skłodowska-Curie Actions, European Union; Investissements d'Avenir Labex, Investissements d'Avenir Idex and ANR, France; DFG and AvH Foundation, Germany; Herakleitos, Thales and Aristeia programmes co-financed by EU-ESF and the Greek NSRF, Greece; BSF-NSF and MINERVA, Israel; Norwegian Financial Mechanism 2014-2021, Norway; NCN and NAWA, Poland; La Caixa Banking Foundation, CERCA Programme Generalitat de Catalunya and PROMETEO and GenT Programmes Generalitat Valenciana, Spain; Göran Gustafssons Stiftelse, Sweden; The Royal Society and Leverhulme Trust, United Kingdom.

The crucial computing support from all WLCG partners is acknowledged gratefully, in particular from CERN, the ATLAS Tier-1 facilities at TRIUMF (Canada), NDGF (Denmark, Norway, Sweden), CC-IN2P3 (France), KIT/GridKA (Germany), INFN-CNAF (Italy), NL-T1 (Netherlands), PIC (Spain), ASGC (Taiwan), RAL (UK) and BNL (USA), the Tier-2 facilities worldwide and large non-WLCG resource providers. Major contributors of computing resources are listed in Ref. [91].

References

[1] N. Arkani-Hamed, S. Dimopoulos, and G. Dvali, *The hierarchy problem and new dimensions at a millimeter*, Phys. Lett. B **429** (1998) 263, arXiv: hep-ph/9803315 (cit. on p. 2).

[2] I. Antoniadis, N. Arkani-Hamed, S. Dimopoulos, and G. Dvali, *New dimensions at a millimeter to a fermi and superstrings at a TeV*, Phys. Lett. B **436** (1998) 257, arXiv: hep-ph/9804398 (cit. on p. 2).

[3] L. Randall and R. Sundrum, *Large Mass Hierarchy from a Small Extra Dimension*, Phys. Rev. Lett. **83** (1999) 3370, arXiv: hep-ph/9905221 (cit. on p. 2).

[4] P. Meade and L. Randall, *Black holes and quantum gravity at the LHC*, JHEP **05** (2008) 003, arXiv: 0708.3017 [hep-ph] (cit. on p. 2).

[5] X. Calmet, W. Gong, and S. D. H. Hsu, *Colorful quantum black holes at the LHC*, Phys. Lett. **B668** (2008) 20, arXiv: 0806.4605 [hep-ph] (cit. on p. 2).

[6] D. M. Gingrich, *Quantum black holes with charge, color and spin at the LHC*, J. Phys. G **37** (2010) 105008, arXiv: 0912.0826 [hep-ph] (cit. on p. 2).

[7] L. A. Anchordoqui, J. L. Feng, H. Goldberg, and A. D. Shapere, *Black holes from cosmic rays: Probes of extra dimensions and new limits on TeV-scale gravity*, Phys. Rev. **D65** (2002) 124027, arXiv: hep-ph/0112247 (cit. on p. 2).

[8] ATLAS Collaboration, *Search for strong gravity in multijet final states produced in pp collisions at $\sqrt{s} = 13$ TeV using the ATLAS detector at the LHC*, JHEP **03** (2016) 026, arXiv: 1512.02586 [hep-ex] (cit. on p. 2).

[9] ATLAS Collaboration, *Search for heavy particles decaying into top-quark pairs using lepton-plus-jets events in proton–proton collisions at $\sqrt{s} = 13$ TeV with the ATLAS detector*, Eur. Phys. J. C **78** (2018) 565, arXiv: 1804.10823 [hep-ex] (cit. on p. 2).

[10] CMS Collaboration, *Search for black holes and other new phenomena in high-multiplicity final states in proton–proton collisions at $\sqrt{s} = 13$ TeV*, Phys. Lett. B **774** (2017) 279, arXiv: 1705.01403 [hep-ex] (cit. on p. 2).

[11] CMS Collaboration, *Search for black holes and sphalerons in high-multiplicity final states in proton–proton collisions at $\sqrt{s} = 13$ TeV*, JHEP **11** (2018) 042, arXiv: 1805.06013 [hep-ex] (cit. on p. 2).

[12] ATLAS Collaboration, *Search for Quantum Black Hole Production in High-Invariant-Mass Lepton+Jet Final States Using pp Collisions at $\sqrt{s} = 8$ TeV and the ATLAS Detector*, Phys. Rev. Lett. **112** (2014) 091804, arXiv: 1311.2006 [hep-ex] (cit. on pp. 2, 5, 7, 16).

[13] ATLAS Collaboration, *A search for new physics in dijet mass and angular distributions in pp collisions at $\sqrt{s} = 7$ TeV measured with the ATLAS detector*, New J. Phys. **13** (2011) 053044, arXiv: 1103.3864 [hep-ex] (cit. on p. 3).

[14] ATLAS Collaboration, *ATLAS search for new phenomena in dijet mass and angular distributions using pp collisions at $\sqrt{s} = 7$ TeV*, JHEP **01** (2013) 029, arXiv: 1210.1718 [hep-ex] (cit. on p. 3).

[15] CMS Collaboration, *Search for narrow resonances and quantum black holes in inclusive and b-tagged dijet mass spectra from pp collisions at $\sqrt{s} = 7$ TeV*, JHEP **01** (2013) 013, arXiv: 1210.2387 [hep-ex] (cit. on p. 3).

[16] ATLAS Collaboration, *Search for new phenomena in photon+jet events collected in proton–proton collisions at $\sqrt{s} = 8$ TeV with the ATLAS detector*, Phys. Lett. B **728** (2014) 562, arXiv: 1309.3230 [hep-ex] (cit. on p. 3).

[17] ATLAS Collaboration, *Search for high-mass dilepton resonances in pp collisions at $\sqrt{s} = 8$ TeV with the ATLAS detector*, Phys. Rev. D **90** (2014) 052005, arXiv: 1405.4123 [hep-ex] (cit. on p. 3).

[18] ATLAS Collaboration, *Search for new phenomena in the dijet mass distribution using pp collision data at $\sqrt{s} = 8$ TeV with the ATLAS detector*, Phys. Rev. D **91** (2015) 052007, arXiv: 1407.1376 [hep-ex] (cit. on p. 3).

[19] CMS Collaboration, *Search for resonances and quantum black holes using dijet mass spectra in proton–proton collisions at $\sqrt{s} = 8$ TeV*, Phys. Rev. D **91** (2015) 052009, arXiv: 1501.04198 [hep-ex] (cit. on p. 3).

[20] ATLAS Collaboration, *Search for new phenomena in final states with an energetic jet and large missing transverse momentum in pp collisions at $\sqrt{s} = 8$ TeV with the ATLAS detector*, Eur. Phys. J. C **75** (2015) 299, arXiv: 1502.01518 [hep-ex] (cit. on p. 3).

[21] ATLAS Collaboration, *Search for new phenomena in dijet mass and angular distributions from pp collisions at $\sqrt{s} = 13$ TeV with the ATLAS Detector*, Phys. Lett. B **754** (2016) 302, arXiv: 1512.01530 [hep-ex] (cit. on p. 3).

[22] ATLAS Collaboration, *Search for new phenomena in different-flavour high-mass dilepton final states in pp collisions at $\sqrt{s} = 13$ TeV with the ATLAS detector*, Eur. Phys. J. C **76** (2016) 541, arXiv: 1607.08079 [hep-ex] (cit. on p. 3).

[23] CMS Collaboration, *Search for new physics with dijet angular distributions in proton–proton collisions at $\sqrt{s} = 13$ TeV*, JHEP **07** (2017) 013, arXiv: 1703.09986 [hep-ex] (cit. on p. 3).

[24] CMS Collaboration, *Search for lepton-flavor violating decays of heavy resonances and quantum black holes to $e\mu$ final states in proton–proton collisions at $\sqrt{s} = 13$ TeV*, JHEP **04** (2018) 073, arXiv: 1802.01122 [hep-ex] (cit. on p. 3).

[25] ATLAS Collaboration, *Search for new resonances in mass distributions of jet pairs using 139 fb^{-1} of pp collisions at $\sqrt{s} = 13$ TeV with the ATLAS detector*, JHEP **03** (2019) 145, arXiv: 1910.08447 [hep-ex] (cit. on p. 3).

[26] ATLAS Collaboration, *The ATLAS Experiment at the CERN Large Hadron Collider*, JINST **3** (2008) S08003 (cit. on p. 3).

[27] B. Abbott et al., *Production and integration of the ATLAS Insertable B-Layer*, JINST **13** (2018) T05008, arXiv: 1803.00844 [physics.ins-det] (cit. on p. 3).

[28] ATLAS Collaboration, *Performance of the ATLAS trigger system in 2015*, Eur. Phys. J. C **77** (2017) 317, arXiv: 1611.09661 [hep-ex] (cit. on p. 3).

[29] ATLAS Collaboration, *The ATLAS Collaboration Software and Firmware*, ATL-SOFT-PUB-2021-001, 2021, URL: https://cds.cern.ch/record/2767187 (cit. on p. 3).

[30] ATLAS Collaboration, *ATLAS data quality operations and performance for 2015–2018 data-taking*, JINST **15** (2019) P04003, arXiv: 1911.04632 [physics.ins-det] (cit. on p. 3).

[31] ATLAS Collaboration, *Performance of electron and photon triggers in ATLAS during LHC Run 2*, Eur. Phys. J. C **80** (2019) 47, arXiv: 1909.00761 [hep-ex] (cit. on pp. 3, 9).

[32] ATLAS Collaboration, *Performance of the ATLAS muon triggers in Run 2*, JINST **15** (2020) P09015, arXiv: 2004.13447 [physics.ins-det] (cit. on p. 3).

[33] ATLAS Collaboration, *Luminosity determination in pp collisions at $\sqrt{s} = 13$ TeV using the ATLAS detector at the LHC*, submitted to EPJC (2022), arXiv: 2212.09379 [hep-ex], URL: https://cds.cern.ch/record/2844887 (cit. on pp. 3, 10).

[34] G. Avoni et al., *The new LUCID-2 detector for luminosity measurement and monitoring in ATLAS*, JINST **13** (2018) P07017 (cit. on p. 3).

[35] ATLAS Collaboration, *Multi-Boson Simulation for 13 TeV ATLAS Analyses*, ATL-PHYS-PUB-2017-005, 2017, URL: https://cds.cern.ch/record/2261933 (cit. on p. 4).

[36] ATLAS Collaboration, *ATLAS simulation of boson plus jets processes in Run 2*, ATL-PHYS-PUB-2017-006, 2017, URL: https://cds.cern.ch/record/2261937 (cit. on p. 4).

[37] E. Bothmann et al., *Event generation with Sherpa 2.2*, SciPost Phys. **7** (2019) 034, arXiv: 1905.09127 [hep-ph] (cit. on p. 4).

[38] T. Gleisberg and S. Höche, *Comix, a new matrix element generator*, JHEP **12** (2008) 039, arXiv: 0808.3674 [hep-ph] (cit. on p. 4).

[39] S. Schumann and F. Krauss, *A parton shower algorithm based on Catani–Seymour dipole factorisation*, JHEP **03** (2008) 038, arXiv: 0709.1027 [hep-ph] (cit. on p. 4).

[40] R. D. Ball et al., *Parton distributions for the LHC Run II*, JHEP **04** (2015) 040, arXiv: 1410.8849 [hep-ph] (cit. on pp. 4, 10).

[41] S. Höche, F. Krauss, M. Schönherr, and F. Siegert, *A critical appraisal of NLO+PS matching methods*, JHEP **09** (2012) 049, arXiv: 1111.1220 [hep-ph] (cit. on p. 4).

[42] S. Höche, F. Krauss, M. Schönherr, and F. Siegert, *QCD matrix elements + parton showers. The NLO case*, JHEP **04** (2013) 027, arXiv: 1207.5030 [hep-ph] (cit. on p. 4).

[43] S. Catani, F. Krauss, B. R. Webber, and R. Kuhn, *QCD Matrix Elements + Parton Showers*, JHEP **11** (2001) 063, arXiv: hep-ph/0109231 (cit. on p. 4).

[44] S. Höche, F. Krauss, S. Schumann, and F. Siegert, *QCD matrix elements and truncated showers*, JHEP **05** (2009) 053, arXiv: 0903.1219 [hep-ph] (cit. on p. 4).

[45] F. Cascioli, P. Maierhöfer, and S. Pozzorini, *Scattering Amplitudes with Open Loops*, Phys. Rev. Lett. **108** (2012) 111601, arXiv: 1111.5206 [hep-ph] (cit. on p. 4).

[46] A. Denner, S. Dittmaier, and L. Hofer, *Collier: a fortran-based complex one-loop library in extended regularizations*, Comput. Phys. Commun. **212** (2017) 220, arXiv: 1604.06792 [hep-ph] (cit. on p. 4).

[47] C. Anastasiou, L. J. Dixon, K. Melnikov, and F. Petriello, *High precision QCD at hadron colliders: Electroweak gauge boson rapidity distributions at next-to-next-to leading order*, Phys. Rev. D **69** (2004) 094008, arXiv: hep-ph/0312266 (cit. on p. 4).

[48] M. Grazzini, S. Kallweit, and D. Rathlev, *ZZ production at the LHC: fiducial cross sections and distributions in NNLO QCD*, Phys. Lett. **B750** (2015) 407, arXiv: 1507.06257 [hep-ph] (cit. on p. 4).

[49] S. Frixione, P. Nason, and G. Ridolfi, *A positive-weight next-to-leading-order Monte Carlo for heavy flavour hadroproduction*, JHEP **09** (2007) 126, arXiv: `0707.3088 [hep-ph]` (cit. on p. 4).

[50] E. Re, *Single-top Wt-channel production matched with parton showers using the POWHEG method*, Eur. Phys. J. C **71** (2011) 1547, arXiv: `1009.2450 [hep-ph]` (cit. on p. 4).

[51] S. Alioli, P. Nason, C. Oleari, and E. Re, *NLO single-top production matched with shower in POWHEG: s- and t-channel contributions*, JHEP **09** (2009) 111, arXiv: `0907.4076 [hep-ph]`, Erratum: JHEP **02** (2010) 011 (cit. on p. 4).

[52] P. Nason, *A new method for combining NLO QCD with shower Monte Carlo algorithms*, JHEP **11** (2004) 040, arXiv: `hep-ph/0409146` (cit. on p. 4).

[53] S. Frixione, P. Nason, and C. Oleari, *Matching NLO QCD computations with parton shower simulations: the POWHEG method*, JHEP **11** (2007) 070, arXiv: `0709.2092 [hep-ph]` (cit. on p. 4).

[54] S. Alioli, P. Nason, C. Oleari, and E. Re, *A general framework for implementing NLO calculations in shower Monte Carlo programs: the POWHEG BOX*, JHEP **06** (2010) 043, arXiv: `1002.2581 [hep-ph]` (cit. on p. 4).

[55] R. Frederix, E. Re, and P. Torrielli, *Single-top t-channel hadroproduction in the four-flavour scheme with POWHEG and aMC@NLO*, JHEP **09** (2012) 130, arXiv: `1207.5391 [hep-ph]` (cit. on p. 4).

[56] T. Sjöstrand et al., *An introduction to PYTHIA 8.2*, Comput. Phys. Commun. **191** (2015) 159, arXiv: `1410.3012 [hep-ph]` (cit. on p. 4).

[57] ATLAS Collaboration, *ATLAS Pythia 8 tunes to* 7 *TeV data*, ATL-PHYS-PUB-2014-021, 2014, URL: `https://cds.cern.ch/record/1966419` (cit. on p. 4).

[58] R. D. Ball et al., *Parton distributions with LHC data*, Nucl. Phys. B **867** (2013) 244, arXiv: `1207.1303 [hep-ph]` (cit. on p. 4).

[59] ATLAS Collaboration, *Studies on top-quark Monte Carlo modelling for Top2016*, ATL-PHYS-PUB-2016-020, 2016, URL: `https://cds.cern.ch/record/2216168` (cit. on p. 4).

[60] M. Czakon and A. Mitov, *Top++: A program for the calculation of the top-pair cross-section at hadron colliders*, Comput. Phys. Commun. **185** (2014) 2930, arXiv: `1112.5675 [hep-ph]` (cit. on p. 4).

[61] M. Aliev et al., *HATHOR: HAdronic Top and Heavy quarks crOss section calculatoR*, Comput. Phys. Commun. **182** (2011) 1034, arXiv: `1007.1327 [hep-ph]` (cit. on p. 4).

[62] P. Kant et al., *HatHor for single top-quark production: Updated predictions and uncertainty estimates for single top-quark production in hadronic collisions*, Comput. Phys. Commun. **191** (2015) 74, arXiv: `1406.4403 [hep-ph]` (cit. on p. 4).

[63] P. Artoisenet, R. Frederix, O. Mattelaer, and R. Rietkerk, *Automatic spin-entangled decays of heavy resonances in Monte Carlo simulations*, JHEP **03** (2013) 015, arXiv: `1212.3460 [hep-ph]` (cit. on p. 4).

[64] D. J. Lange, *The EvtGen particle decay simulation package*, Nucl. Instrum. Meth. A **462** (2001) 152 (cit. on p. 4).

[65] D. M. Gingrich, *Monte Carlo event generator for black hole production and decay in proton-proton collisions - QBH version 1.02*, Comput. Phys. Commun. **181** (2010) 1917, arXiv: 0911.5370 [hep-ph] (cit. on pp. 4, 5).

[66] D. Stump et al., *Inclusive jet production, parton distributions, and the search for new physics*, JHEP **10** (2003) 046, arXiv: hep-ph/0303013 (cit. on p. 4).

[67] ATLAS Collaboration, *The Pythia 8 A3 tune description of ATLAS minimum bias and inelastic measurements incorporating the Donnachie–Landshoff diffractive model*, ATL-PHYS-PUB-2016-017, 2016, URL: https://cds.cern.ch/record/2206965 (cit. on p. 5).

[68] ATLAS Collaboration, *The ATLAS Simulation Infrastructure*, Eur. Phys. J. C **70** (2010) 823, arXiv: 1005.4568 [physics.ins-det] (cit. on p. 5).

[69] S. Agostinelli et al., *Geant4 – a simulation toolkit*, Nucl. Instrum. Meth. A **506** (2003) 250 (cit. on p. 5).

[70] ATLAS Collaboration, *The simulation principle and performance of the ATLAS fast calorimeter simulation FastCaloSim*, ATL-PHYS-PUB-2010-013, 2010, URL: https://cds.cern.ch/record/1300517 (cit. on p. 5).

[71] ATLAS Collaboration, *Vertex Reconstruction Performance of the ATLAS Detector at $\sqrt{s} = 13$ TeV*, ATL-PHYS-PUB-2015-026, 2015, URL: https://cds.cern.ch/record/2037717 (cit. on p. 5).

[72] ATLAS Collaboration, *Electron and photon performance measurements with the ATLAS detector using the 2015–2017 LHC proton–proton collision data*, JINST **14** (2019) P12006, arXiv: 1908.00005 [hep-ex] (cit. on pp. 5, 6, 9).

[73] ATLAS Collaboration, *Muon reconstruction performance of the ATLAS detector in proton–proton collision data at $\sqrt{s} = 13$ TeV*, Eur. Phys. J. C **76** (2016) 292, arXiv: 1603.05598 [hep-ex] (cit. on pp. 6, 9).

[74] M. Cacciari, G. P. Salam, and G. Soyez, *The anti-k_t jet clustering algorithm*, JHEP **04** (2008) 063, arXiv: 0802.1189 [hep-ph] (cit. on p. 6).

[75] M. Cacciari, G. P. Salam, and G. Soyez, *FastJet user manual*, Eur. Phys. J. C **72** (2012) 1896, arXiv: 1111.6097 [hep-ph] (cit. on p. 6).

[76] ATLAS Collaboration, *Topological cell clustering in the ATLAS calorimeters and its performance in LHC Run 1*, Eur. Phys. J. C **77** (2017) 490, arXiv: 1603.02934 [hep-ex] (cit. on p. 6).

[77] ATLAS Collaboration, *Determination of jet calibration and energy resolution in proton–proton collisions at $\sqrt{s} = 8$ TeV using the ATLAS detector*, (2019), arXiv: 1910.04482 [hep-ex] (cit. on p. 6).

[78] ATLAS Collaboration, *Jet energy scale measurements and their systematic uncertainties in proton–proton collisions at $\sqrt{s} = 13$ TeV with the ATLAS detector*, Phys. Rev. D **96** (2017) 072002, arXiv: 1703.09665 [hep-ex] (cit. on pp. 6, 9).

[79] ATLAS Collaboration, *Selection of jets produced in 13 TeV proton–proton collisions with the ATLAS detector*, ATLAS-CONF-2015-029, 2015, URL: https://cds.cern.ch/record/2037702 (cit. on p. 6).

[80] ATLAS Collaboration, *Performance of pile-up mitigation techniques for jets in pp collisions at $\sqrt{s} = 8$ TeV using the ATLAS detector*, Eur. Phys. J. C **76** (2016) 581, arXiv: 1510.03823 [hep-ex] (cit. on pp. 6, 9).

[81] ATLAS Collaboration, *Measurements of b-jet tagging efficiency with the ATLAS detector using $t\bar{t}$ events at $\sqrt{s} = 13$ TeV*, JHEP **08** (2018) 089, arXiv: 1805.01845 [hep-ex] (cit. on p. 6).

[82] ATLAS Collaboration, *ATLAS b-jet identification performance and efficiency measurement with $t\bar{t}$ events in pp collisions at $\sqrt{s} = 13$ TeV*, Eur. Phys. J. C **79** (2019) 970, arXiv: 1907.05120 [hep-ex] (cit. on p. 6).

[83] ATLAS Collaboration, *Performance of missing transverse momentum reconstruction with the ATLAS detector using proton–proton collisions at $\sqrt{s} = 13$ TeV*, Eur. Phys. J. C **78** (2018) 903, arXiv: 1802.08168 [hep-ex] (cit. on p. 6).

[84] ATLAS Collaboration, *E_T^{miss} performance in the ATLAS detector using 2015–2016 LHC pp collisions*, ATLAS-CONF-2018-023, 2018, URL: https://cds.cern.ch/record/2625233 (cit. on p. 6).

[85] ATLAS Collaboration, *Search for a heavy charged boson in events with a charged lepton and missing transverse momentum from pp collisions at $\sqrt{s} = 13$ TeV with the ATLAS detector*, Phys. Rev. D **100** (2019) 052013, arXiv: 1906.05609 [hep-ex] (cit. on pp. 7, 10).

[86] ATLAS Collaboration, *Tools for estimating fake/non-prompt lepton backgrounds with the ATLAS detector at the LHC*, CERN-EP-2022-214, 2022, arXiv: 2211.16178 [hep-ex], URL: https://cds.cern.ch/record/2842463 (cit. on p. 8).

[87] M. Baak et al., *HistFitter software framework for statistical data analysis*, Eur. Phys. J. C **75** (2015) 153, arXiv: 1410.1280 [hep-ex] (cit. on p. 8).

[88] G. Cowan, K. Cranmer, E. Gross, and O. Vitells, *Asymptotic formulae for likelihood-based tests of new physics*, Eur. Phys. J. C **71** (2011) 1554, arXiv: 1007.1727 [physics.data-an] (cit. on p. 9).

[89] A. L. Read, *Presentation of search results: the CL_S technique*, J. Phys. G **28** (2002) 2693 (cit. on p. 9).

[90] ATLAS Collaboration, *Measurement of the Inelastic Proton–Proton Cross Section at $\sqrt{s} = 13$ TeV with the ATLAS Detector at the LHC*, Phys. Rev. Lett. **117** (2016) 182002, arXiv: 1606.02625 [hep-ex] (cit. on p. 10).

[91] ATLAS Collaboration, *ATLAS Computing Acknowledgements*, ATL-SOFT-PUB-2021-003, URL: https://cds.cern.ch/record/2776662 (cit. on p. 16).

Auxiliary material

Table 6: Fitted background normalization factors from the simultaneous *background-only* fit in three CRs for the electron+jet and muon+jet channels.

Background	electron+jet	muon+jet
W+jets	1.010 ± 0.021	1.016 ± 0.015
Z+jets	0.972 ± 0.036	0.990 ± 0.032
$t\bar{t}$	0.946 ± 0.061	0.948 ± 0.083

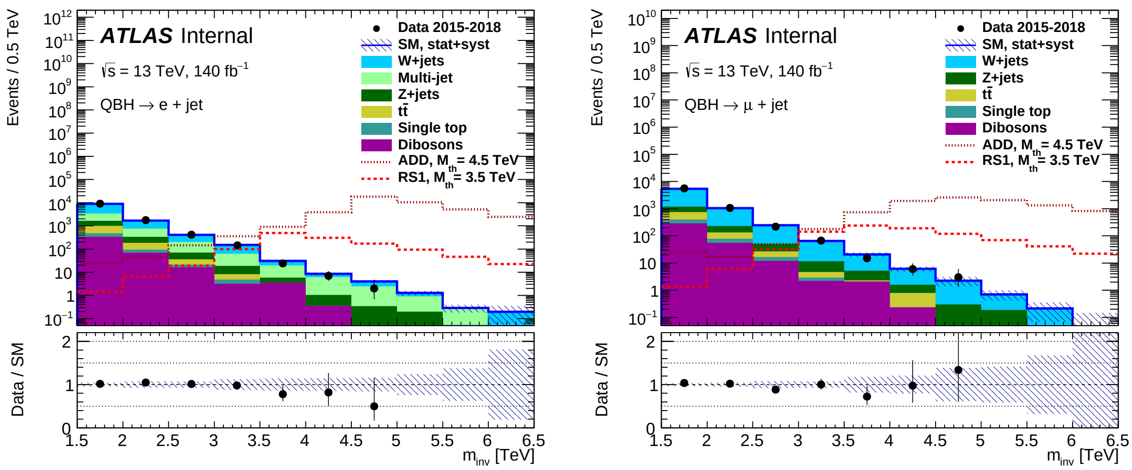

(a) (b)

Figure 5: The event distributions over m_{inv} of a leading lepton and a leading jet in the SVR+SR region with the bin size of 0.5 TeV for data (points with error bars) and for SM backgrounds (solid histograms) after the *background-only* fit are shown in: (a) the electron+jet channel and (b) the muon+jet channel. The normalizations extracted from the fit in the CRs are applied in the full m_{inv} range including the SVR and the SR. The sum of the statistical errors of the MC and systematic uncertainties is shown by the hatched area. The lower panels show ratios of the number of events observed in the data to the total background. The hatched band represents the total relative uncertainty in the background estimate. Two examples of the QBH signals normalized to the predicted cross-section are overlaid.

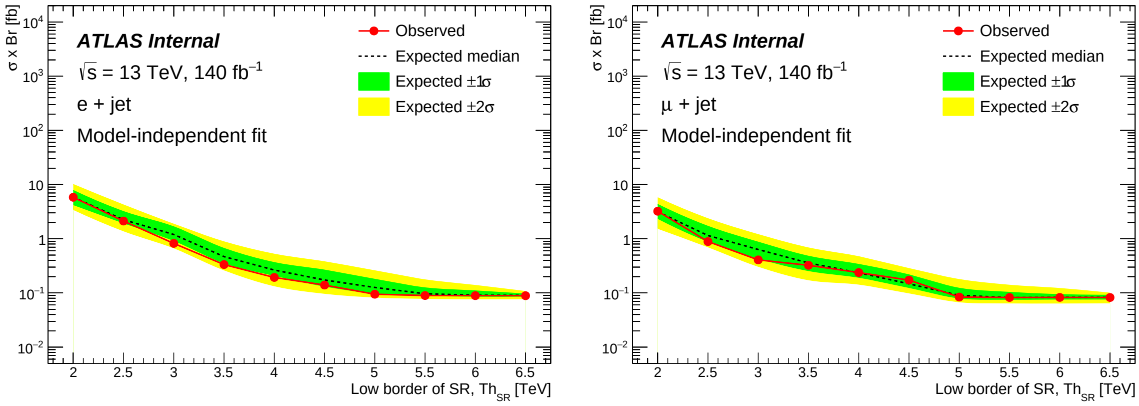

(a) (b)

Figure 6: The 95% C.L. *model-independent* upper limits on $\sigma \times Br$ for the non-SM signal production with decay into: (a) electron+jet and (b) muon+jet. The limits take into account statistical and systematic uncertainties. Circles along the solid red line indicate the lower border of the SR (threshold of the SR, $\mathrm{Th_{SR}}$), above which the observed limit is computed. The expected limits are shown by the dashed line. The $\pm 1\sigma$ and $\pm 2\sigma$ bands of expected limits are shown in green and yellow, respectively. The limits are obtained with pseudo-experiments.

Table 7: *Model-dependent* fit. The observed number of data events, the fitted and expected yields of the SM background and the signal for two models of the ADD (7.0 TeV) and the RS1 (5.0 TeV). Errors include both statistical errors and systematic uncertainties.

	ADD electrons	ADD muons	RS1 electrons	RS1 muons
Observed data	2319	1359	2319	1359
Fitted events	2317 ± 47	1362 ± 29	2317 ± 47	1363 ± 34
W+jets	1314 ± 33	1069 ± 23	1315 ± 33	1068 ± 28
Multi-jet	569 ± 26	–	569 ± 26	–
Z+jets	199 ± 15	127 ± 9	199 ± 15	128 ± 9
$t\bar{t}$	109 ± 7	68 ± 5	109 ± 7	67 ± 4
Single top	31 ± 2	28 ± 2	31 ± 2	28 ± 2
Dibosons	94 ± 8	70 ± 8	94 ± 8	71 ± 9
Signal events	$0.0^{+0.3}_{-0.0}$	$0.0^{+0.4}_{-0.0}$	$0.0^{+0.5}_{-0.0}$	$0.0^{+0.8}_{-0.0}$
Expected events	3850 ± 410	2080 ± 260	2910 ± 120	1480 ± 87
W+jets	1654 ± 65	1016 ± 48	1654 ± 65	1016 ± 48
Multi-jet	577 ± 38	–	577 ± 38	–
Z+jets	186 ± 18	122 ± 12	186 ± 18	122 ± 12
$t\bar{t}$	109 ± 6	66 ± 5	108 ± 6	66 ± 5
Single top	29 ± 2	28 ± 2	29 ± 2	28 ± 2
Dibosons	92 ± 10	66 ± 8	92 ± 10	66 ± 8
Signal events	1210 ± 400	780 ± 250	264 ± 82	182 ± 58

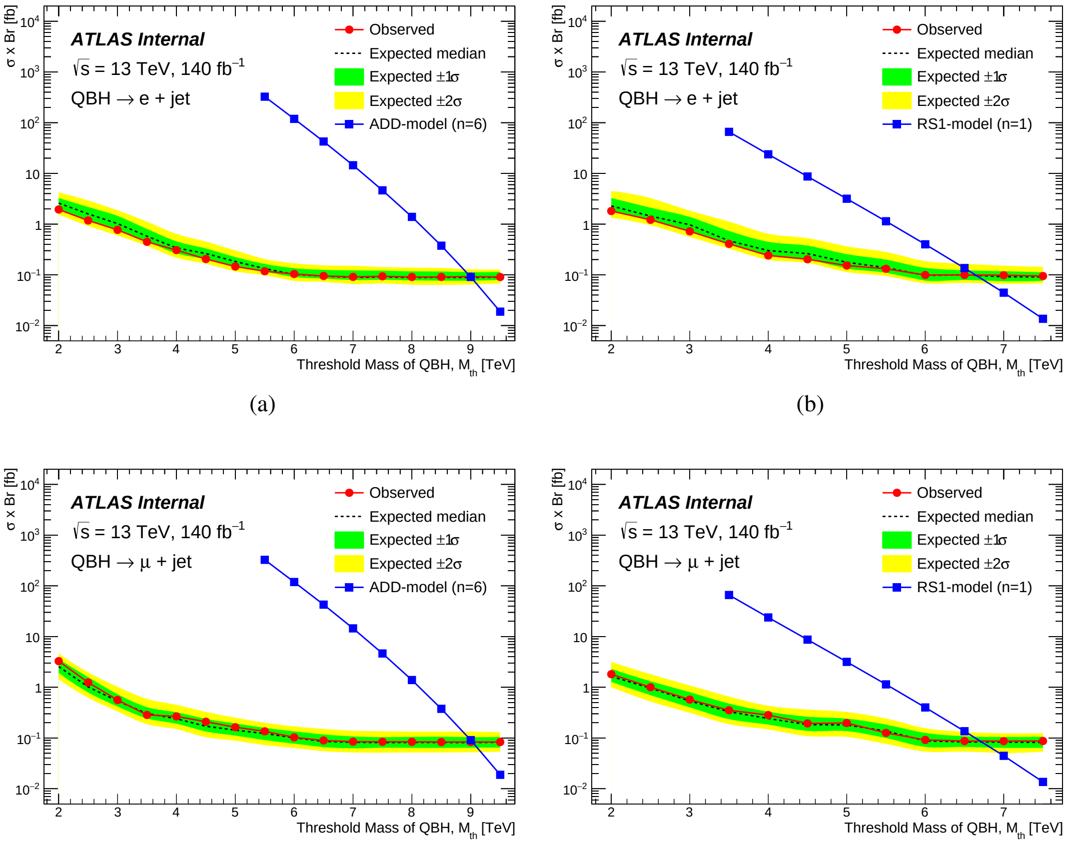

(a) (b) (c) (d)

Figure 7: The 95% C.L. upper limits on $\sigma \times Br$ as a function of M_{th} for QBH production at $M_{\text{th}} = M_{\text{D}}$ with decay into: (a, b) electron+jet and (c, d) muon+jet. (a, c) show limits for the ADD-model (extra dimensions $n = 6$) and (b, d) for the RS1-model (extra dimensions $n = 1$). The limits take into account statistical and systematic uncertainties. Circles along the solid red line indicate the M_{th} mass of the signal where the observed limit is computed. The expected limits are shown by the dashed line. The $\pm 1\sigma$ and $\pm 2\sigma$ bands are shown in green and yellow, respectively. The theoretically predicted $\sigma \times Br$ for the QBH production and decay is shown as the solid blue curve with squares.